Multi-function and generalized intelligent code-bench based on Monte Carlo method (MagicMC) for nuclear applications

Zhen-Ping Chen[1,2] · Ai-Kou Sun[1,2] · Ji-Chong Lei[1,2] · Cheng-Wei Liu[1,2] · Yi-Qing Zhang[1,2] · Chao Yang[1,2] · Jin-Sen Xie[1,2] · Tao Yu[1,2]

Abstract

The Monte Carlo (MC) method offers significant advantages in handling complex geometries and physical processes in particle transport problems and has become a widely used approach in reactor physics analysis, radiation shielding design, and medical physics. However, with the rapid advancement of new nuclear energy systems, the Monte Carlo method faces challenges in efficiency, accuracy, and adaptability, limiting its effectiveness in meeting modern design requirements. Overcoming technical obstacles related to high-fidelity coupling, high-resolution computation, and intelligent design is essential for using the Monte Carlo method as a reliable tool in numerical analysis for these new nuclear energy systems. To address these challenges, the Nuclear Energy and Application Laboratory (NEAL) team at the University of South China developed a multifunctional and generalized intelligent code platform called MagicMC, based on the Monte Carlo particle transport method. MagicMC is a developing tool dedicated to nuclear applications, incorporating intelligent methodologies. It consists of two primary components: a basic unit and a functional unit. The basic unit, which functions similarly to a standard Monte Carlo particle transport code, includes seven modules: geometry, source, transport, database, tally, output, and auxiliary. The functional unit builds on the basic unit by adding functional modules to address complex and diverse applications in nuclear analysis. MagicMC introduces a dynamic Monte Carlo particle transport algorithm to address time-space particle transport problems within emerging nuclear energy systems and incorporates a CPU-GPU heterogeneous parallel framework to enable high-efficiency, high-resolution simulations for large-scale computational problems. Anticipating future trends in intelligent design, MagicMC integrates several advanced features, including CAD-based geometry modeling, global variance reduction methods, multi-objective shielding optimization, high-resolution activation analysis, multi-physics coupling, and radiation therapy. In this paper, various numerical benchmarks-spanning reactor transient simulations, material activation analysis, radiation shielding optimization, and medical dosimetry analysis-are presented to validate MagicMC. The numerical results demonstrate MagicMC's efficiency, accuracy, and reliability in these preliminary applications, underscoring its potential to support technological advancements in developing high-fidelity, high-resolution, and high-intelligence MC-based tools for advanced nuclear applications.

Keywords Monte Carlo · Particle transport · Intelligent design · Nuclear application

✉ Tao Yu
yutao29@sina.com

1 School of Nuclear Science and Technology, University of South China, Hengyang 421001, China

2 Key Lab of Advanced Nuclear Energy Design and Safety, Ministry of Education, University of South China, Hengyang 421001, China

1 Introduction

With rapid advancements in computer science, the Monte Carlo (MC) method has become widely used across various fields, including financial engineering, economics, biomedical

science, computational physics, aerodynamics, machine learning, and reactor physics [1–3]. In reactor physics, the MC method offers significant advantages for solving particle transport problems, as it effectively manages complex geometries and detailed physical processes. This capability is essential for reactor core physics design, radiation shielding analysis, and medical physics. To meet the diverse requirements across these applications, a range of MC particle transport calculation codes have been developed, such as MCNP, Serpent, Geant, FLUKA, OpenMC, PHITS, RMC, JMCT, TopMC, SuperMC, and MCX [4–10]. The Nuclear Energy and Application Laboratory (NEAL) team at the University of South China has independently developed MagicMC (Multi-function and Generalized Intelligent Code-bench based on the Monte Carlo method). This tool focuses on high-fidelity simulation of nuclear reactor physics, radiation transport calculations, time-dependent particle transport problems, dosimetry physics, and other specialized applications. This paper introduces the architecture, modules, and functionalities of MagicMC and validates its reliability through typical applications.

2 Monte Carlo particle transport theory

The MC method, which gained prominence in the 1940 s and is also known as the random simulation or statistical experiment method, relies on transforming problem-solving into estimating the probability of random events. By conducting a large number of trial samplings, the average probability is calculated to address the problem at hand [11, 12]. Initially, due to limited computing resources, the MC method was mainly used to complement deterministic methods for tackling complex geometrical problems. Monte Carlo particle transport simulation is grounded in probability and statistical theory, establishing the random path of individual particles in a specified geometric system and simulating each step from particle generation to disappearance. The trajectory of a particle within the system is described by a set of state parameters, typically including time variable t, spatial position $\mathbf{r}$, energy E, and flying direction Ω denoted as $S = (t, \mathbf{r}, E, \Omega)$. A source particle moves randomly through the system, undergoing multiple collisions with different nuclei until its journey concludes (e.g., through absorption by a nucleus or escape from the system). The entire particle history within the system is thus represented by a sequence of particle states as follows (1):

$$\begin{pmatrix} t_0, & t_1, & \cdots, & t_{M-1}, & t_M \\ r_0, & r_1, & \cdots, & r_{M-1}, & r_M \\ E_0, & E_1, & \cdots, & E_{M-1}, & E_M \\ \Omega_0, & \Omega_1, & \cdots, & \Omega_{M-1}, & \Omega_M \end{pmatrix} \tag{1}$$

By performing statistical simulations and analyses across numerous particle histories, the Monte Carlo (MC) method

uses statistical averaging to predict and estimate expected values, effectively solving particle transport problems. In particle transport calculations, the MC method offers significant advantages over deterministic methods in the following areas: (1) simplicity and efficiency. The MC method is a straightforward, flexible, and scalable approach. When applied to physical problems, it simplifies complex models by breaking them down into sets of basic events, allowing the encoding of behavior models through specific rules. Furthermore, due to the temporal independence of its events, all event chains in the MC method can theoretically be computed in parallel, aligning with modern trends in computer science. (2) Randomness. The inherent randomness of the MC method is key to accurately simulating real random systems and provides substantial advantages in deterministic numerical calculations. For example, in random optimization, the MC method's randomness naturally helps it avoid local optima, allowing a more comprehensive exploration of the data space-an advantage often absent in deterministic algorithms. (3) Theoretical reliability. An extensive and growing body of mathematical and statistical examples supports the reliability of the MC method. The computational efficiency and errors produced by a model using the MC method can be accurately estimated, and errors can be minimized by increasing the number of particle histories or by applying other mathematical techniques. However, with the rapid development of new nuclear energy systems, the Monte Carlo method, in its current form, can be inefficient and may lack the accuracy and intelligence required to meet design requirements. Addressing the technical challenges of high-fidelity coupling, high-resolution computation, and intelligent design is essential when using the Monte Carlo method as a tool for numerical analysis in next-generation nuclear systems. Consequently, this study introduces MagicMC, a code-bench developed to tackle these challenges with innovative solutions.

3 Architectures of MagicMC code-bench

MagicMC is based on the Monte Carlo particle transport method and is tailored for various intelligent applications. The code-bench was developed in C++, incorporating several extensible functions, supporting Python API functions, and enabling easy expansion and maintenance. MagicMC comprises two main components, as shown in Fig. 1: a basic unit and a functional unit. The basic unit, resembling a standard Monte Carlo particle transport code, consists of seven modules: geometry, source, transport, database, tally, output, and auxiliary. The functional unit builds on the basic unit, incorporating additional functional modules to handle more complex and diverse applications in nuclear analysis. MagicMC implements a dynamic, time-space Monte Carlo

particle transport algorithm designed to solve time-dependent particle transport problems in new nuclear energy systems. Additionally, it features a CPU-GPU heterogeneous parallel framework for efficient, high-resolution simulations for large-scale computational problems.

3.1 Basic unit

3.1.1 Geometry module

This module is primarily used for constructing the geometric structure and material composition of models. It utilizes the constructive solid geometry (CSG) method for geometric descriptions and employs half-space surface methods to build complex computational models, filling the corresponding geometric regions with specified material nuclide compositions and proportions. It also supports ultrafine millimeter-level voxel modeling [13]. Due to the tedious and error-prone nature of manual geometry model creation in MC simulations, this module enables the use of CAD software to construct the geometric input for MagicMC, ensuring consistency between CAD models and MagicMC models. The STEP standard neutral file is used to convert CAD models into MagicMC models [14]. The STEP standard provides a feasible solution for data exchange and sharing between different CAD systems through system-independent neutral files. The specific implementation method is shown in Fig. 2. Firstly, we establish a set of standard modeling processes based on advanced 3D visual modeling platforms. Second, we conduct research on the conversion from boundary representation (BREP) to constructive solid geometry (CSG), constructing three-dimensional solid natural half-spaces and generating characteristic points. Finally, based on the CSG expressions and combined with the surface information of three-dimensional solids, we convert this data into input files for the MagicMC platform.

3.1.2 Source module

This module is designed to establish the initial conditions and properties of particles in general or critical sampling sources, involving time distribution, spatial distribution, angular distribution, and energy distribution. The spatial distribution types are divided into point and volume sources (e.g., rectangular, cylindrical, spherical, and spherical shell sources). Point sources specify particle positions in space using three coordinates (X, Y, and Z). To describe and sample volume sources, spatial location information is required. For example, to uniformly sample source particles in a parallelepiped, the user must specify the diagonal coordinates of
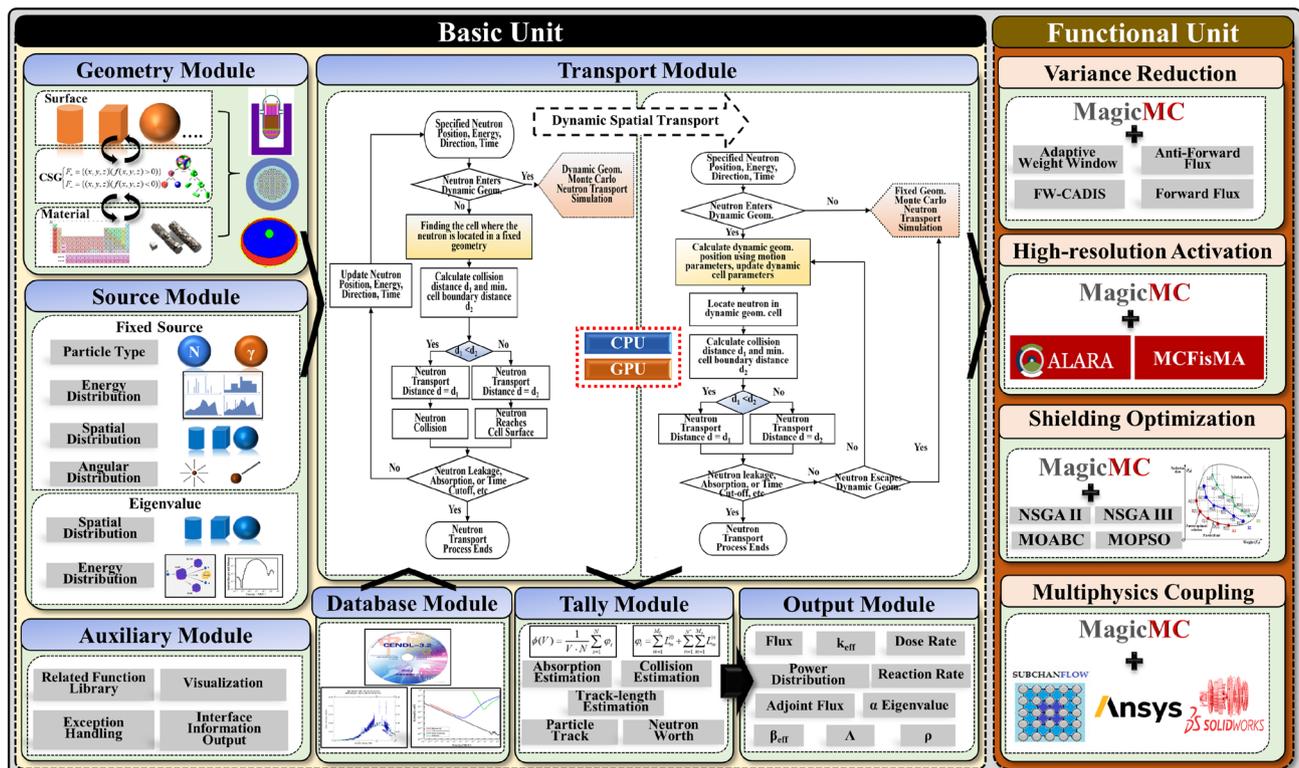

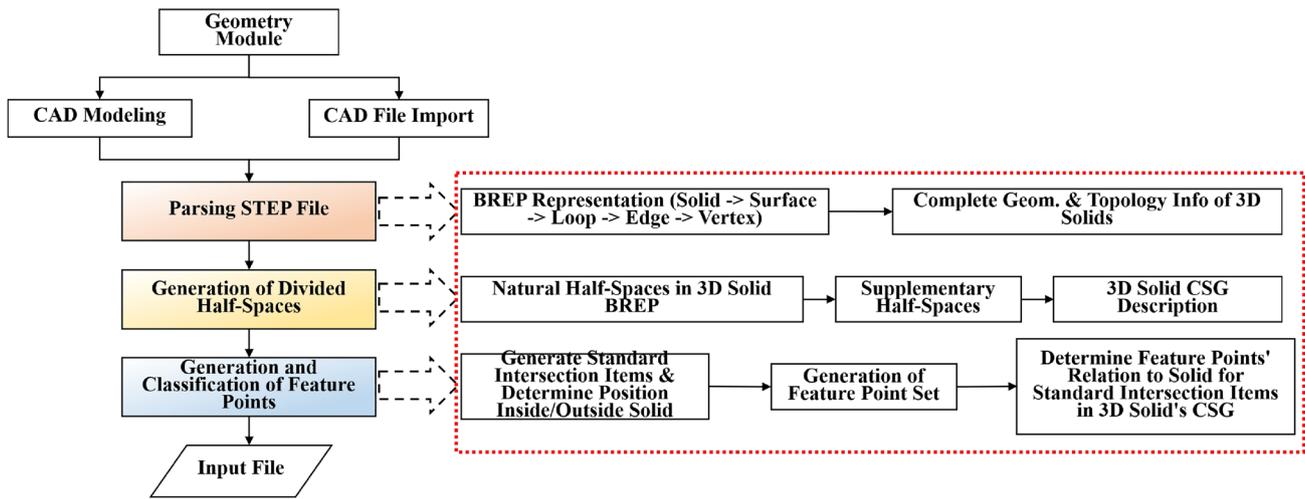**Fig. 1** (Color online) The architecture of MagicMC code-bench

Fig. 2 CAD-based conversion method for the MagicMC model

the body in the input card to define the spatial distribution of the source particles. The particle angular distribution is primarily isotropic or anisotropic and is defined by three parameters: the polar angle ($-1 \leq \cos\theta \leq 1$), azimuthal angle ($0 \leq \phi \leq 2\pi$), and reference vector (u, v, w). Each specific distribution, defined by a probability density function (PDF), has its own sampling method. The energy distribution primarily includes monoenergetic, Watt, Maxwell, discrete, and histogram distributions, where the energy range of incident neutrons is from 0 to 20 MeV, and the energy range of incident photons is from 1 keV to 100 GeV. For a monoenergetic distribution, users set a single fixed value for particle energy (MeV), such as setting the photon energy of ^{137}Cs to 0.662 MeV. The Watt distribution indicates that particle energy follows the Watt fission spectrum, described by the distribution function $p(E)\mathrm{d}E = ce^{-E/a}\sin(bE)^{1/2}\mathrm{d}E$ with parameters a, b. The Maxwell distribution is represented by $p(E)\mathrm{d}E = cE^{1/2}e^{-E/a}\mathrm{d}E$, which requires setting the parameter a. The discrete distribution specifies source energies at discrete points, each with an associated sampling probability. The histogram distribution involves setting each energy bin and its corresponding probability value, with the energy boundary points monotonically increasing. During sampling, the energy bins are first sampled, followed by uniform sampling within the selected energy bin. This method, based on a discrete description of the probability distribution in each energy bin, allows for a more flexible simulation of actual distribution scenarios by dividing the energy range into different bins. Additionally, particle types, such as photons or neutrons, can be set, as shown in Fig. 3.
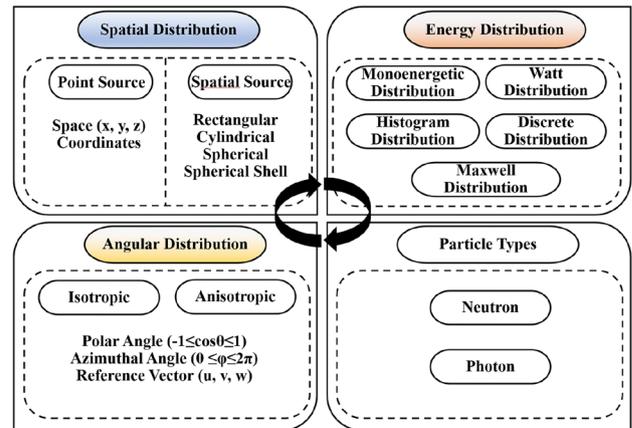

Fig. 3 Parameters definition for source particles

3.1.3 Particle transport module

The particle transport module is the core module of the basic unit, linking upwards to the geometry module, source module, and database module, and supporting the tally and output modules below. The transport module is independently encapsulated and connected through interfaces. This module primarily handles neutron and photon transport calculations. The main particle transport tracking in this section is similar to that of mainstream Monte Carlo programs (Fig. 4) [15–17], and the specific flow is as follows: (i) Perform source particle sampling to determine the initial state of the particle $S_m = (r_m, E_m, \Omega_m)$. The particle departs with this initial state, and the transport length is sampled according to the macroscopic cross section $\Sigma_t(E_m)$ of the material at the current particle collision point to obtain $L = -\ln\zeta/\Sigma_t(E_m)$. (ii) Calculate the distance d from the particle to the nearest

Fig. 4 Particle transport tracking process
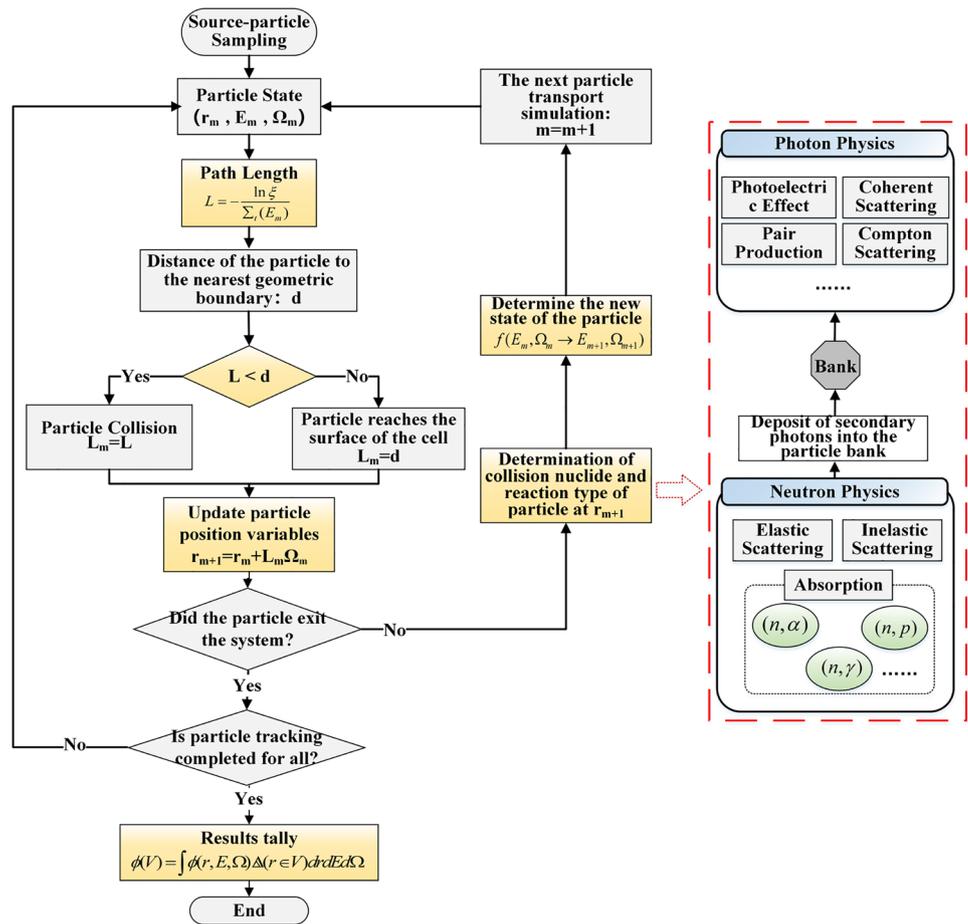
geometric boundary along its direction of motion. (iii) Determine the relationship between the transport length L and the nearest boundary distance d. The position of the $(m + 1)$-th collision is given by $r_{m+1} = r_m + L_m\Omega_m$. (iv) To determine the energy and direction of the particle after a collision, it is necessary to sample the particle interactions to identify the type of reaction occurring with a specific nuclide in the current material. First, using the macroscopic cross sections and total cross section $\Sigma_1, \Sigma_2, \dots, \Sigma_n, \Sigma_t$ of n nuclides in the current material, a random number ζ uniformly distributed in [0, 1] is sampled to identify the interacting nuclide. For example, $0 \le \zeta \le \Sigma_1/\Sigma_t$ indicates that the particle interacts with the first nuclide. After sampling the colliding nuclide, the microscopic cross section σ is used to determine the specific type of interaction between the particle and the current nuclide. The main neutron interactions include elastic scattering, inelastic scattering, and absorption, where absorption is divided into (n, α), (n, p), (n, γ), and (n, f), etc. The total microscopic cross section of a neutron is $\sigma_t = \sigma_e + \sigma_{in} + \sigma_a$, and the type of neutron-matter interaction is determined based on the random number ζ in the range of $[0, \sigma_e/\sigma_t]$, $[\sigma_e/\sigma_t, \sigma_e + \sigma_{in}/\sigma_t]$, and $[\sigma_e + \sigma_{in}/\sigma_t, 1]$ for neutron elastic scattering, inelastic scattering, and absorption, respectively,

with the current nuclide. Photon-matter interaction types include the photoelectric effect, electron-pair production, and Compton scattering, with similar determination methods. (v) After determining the colliding nuclide and type of reaction, the energy and direction of the particle $f(E_m, \Omega_m \to E_{m+1}, \Omega_{m+1})$ can be established.

(1) Dynamic Monte Carlo particle transport method

During nuclear reactor operations, transient processes such as power regulation and rod ejection accidents cause changes in geometry models, which usually cannot be simulated with conventional Monte Carlo codes. Based on the MagicMC Monte Carlo simulation framework, the dynamic behaviors of moving geometric components in the reactor can be modeled in real-time by updating the spatial positions of dynamic geometric components according to the particle time-state parameters. The specific implementation involves updating the dynamic geometric lattice elements, corresponding to vector VVV and rotation matrix RRR, based on the neutron time variables and dynamic geometric motion parameters (translation direction, translation speed, rotation direction, rotation speed,

etc.). In MagicMC, particle tracking is divided into two categories: tracking in dynamic geometries and tracking in fixed geometries. The tracking process in a fixed geometry is similar to that in standard Monte Carlo codes. For tracking in a dynamic geometry, the positions of geometric cells are first updated based on the motion parameters of the dynamic components. The particle tracking process then proceeds similarly to that of standard Monte Carlo codes. This process is illustrated in Fig. 5.

(2) CPU-GPU heterogeneous parallel transport method

With the development of new nuclear reactors, high-fidelity and high-resolution modeling methods have become increasingly important. For reactor transients and multiphysics problems, the computational requirements for achieving satisfactory solutions using the Monte Carlo method are quite expensive, and the central processing unit (CPU) computing resources on personal computers have gradually become insufficient. Unlike standard Monte Carlo codes with history-based transport algorithms, MagicMC employs a stack-driven event-based transport algorithm to enable GPU parallelization. The event-based particle transport algorithm divides the entire transport computation into various types of events, including source sampling, cross-sectional calculations, particle forward distance, collision, surface penetration, particle termination, and particle revival events. Based on the type of the next event each particle must process, multiple active particles are distributed into corresponding stacks. Different stack events are executed in order; the stack length of the event is determined before each event starts, and the longest stack event is selected for calculation until the stack is empty. In subsequent iterations, the longest stack event is selected for computation until the stack is empty. At this point, new particle events are emitted into the event stack, and the entire process is repeated until all event stacks are empty, thereby ending the program. By parallel processing particles undergoing the same events, thread divergence is minimized, and GPU memory utilization is maximized. This allows more particles to be tracked simultaneously, significantly reducing computational time, as shown in Fig. 6 [18, 19].
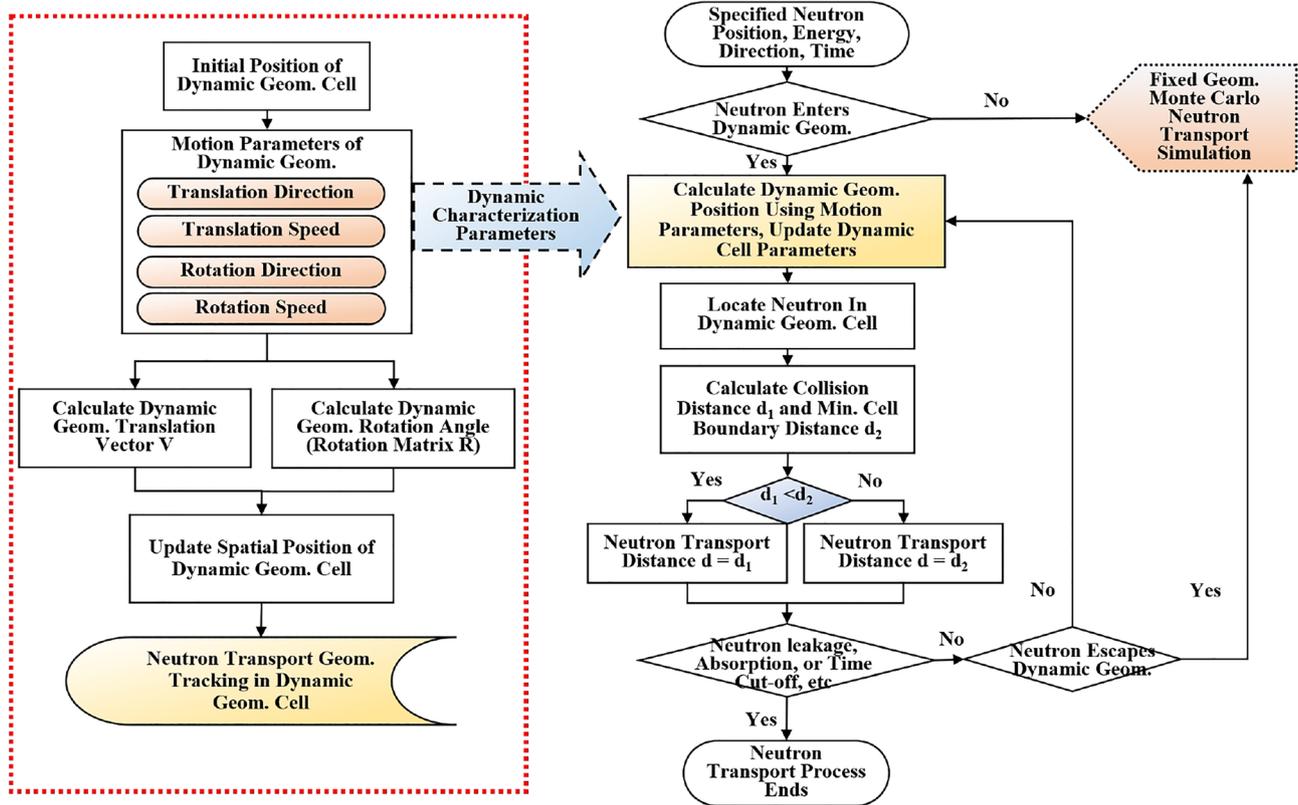

Fig. 5 Particle tracking method in MagicMC

3.1.4 Database module

This module stores nuclear data cross sections essential for reactor physics and radiation shielding design calculations, primarily based on the CENDL database, and is also compatible with other databases like JENDL and ENDF. It includes microscopic cross sections for nuclear reactions induced by neutrons across various energy ranges with various nuclides, angular distributions of neutrons for elastic and inelastic scattering, yields, and energy spectra for prompt and delayed fission neutrons, and thermal neutron scattering $S(\alpha, \beta)$ data for moderators. It also contains cross-sectional data for photon interactions, including the photoelectric effect, Compton effect, and pair production. For activation analysis, the activation database includes cross-sectional data, uncertainty data for neutron-induced reactions, decay data, fission product yield data from neutron-induced reactions, and γ absorption data. For calculations such as reactor depletion analysis and spent fuel composition analysis, the module also includes the corresponding depletion chain library, detailed isotopic transformations, and decay channels over time. For medical dosimetry calculations in BNCT, a library of 106 human tissue compositions from ICRU reports and the corresponding Kerma factor library were created and stored, with functionalities to modify and edit the related data.

3.1.5 Tally module

The tallies module primarily accounts for each particle's contribution to the expected solution during its motion, calculating and solving flux density using collision estimation, track length estimation, and absorption estimation methods. Specifically, MagicMC solves for the dynamic parameters and adjoint flux in critical systems by approximating the iterated fission probability using the number of fission neutrons from the last generation of neutrons. By considering first-generation neutrons as source neutrons and tallying all fission neutrons produced by the last generation in the tallies module, the neutron worth of the source neutrons can be obtained. Eventually, by dividing the neutron worth of the source neutrons by the number of source neutrons in the corresponding region and energy group, the iterated fission probability-approximately equal to the adjoint flux-can be obtained. After obtaining the adjoint flux for each region and energy group, the effective delayed neutron fraction β_{eff} and the neutron generation time Λ are calculated.
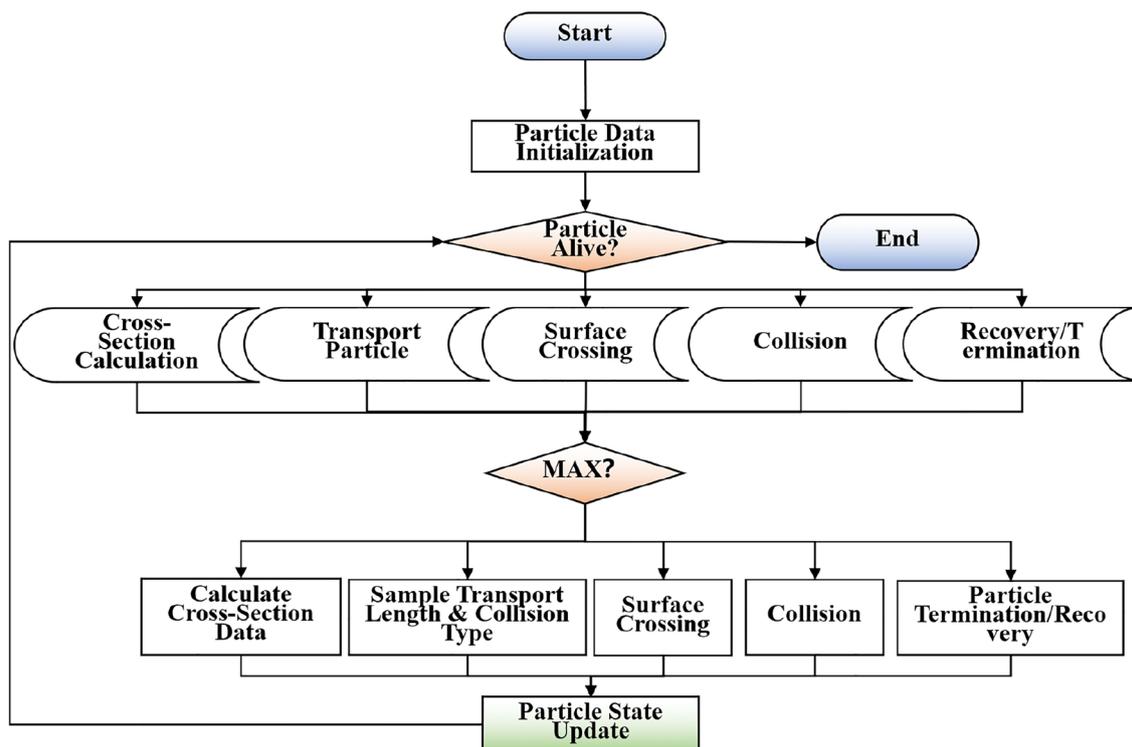

Fig. 6 CPU-GPU heterogeneous parallel Monte Carlo particle transport method

$$\beta_{\text{eff}} = \frac{\sum_i \sum_m \int \phi^*(r,E,\Omega)\chi_{\mathrm{d}i}^m(r,E)u_{\mathrm{d}i}^m(r,E') \cdot \Sigma_\mathrm{f}^m(r,E')\phi(r,E',\Omega')\mathrm{d}\Omega'\mathrm{d}E'\mathrm{d}\Omega\mathrm{d}E\mathrm{d}r}{\sum_m \int \phi^*(r,E,\Omega)\chi_\mathrm{t}^m(r,E)u_\mathrm{t}^m(r,E') \cdot \Sigma_\mathrm{f}^m(r,E')\phi(r,E',\Omega')\mathrm{d}\Omega'\mathrm{d}E'\mathrm{d}\Omega\mathrm{d}E\mathrm{d}r} \tag{2}$$

$$\Lambda = \frac{\int \phi^*(r,E,\Omega)\phi(r,E,\Omega)/v(r,E)\mathrm{d}\Omega\mathrm{d}E\mathrm{d}r}{\sum_m \int \phi^*(r,E,\Omega)\chi_\mathrm{t}^m(r,E)u_\mathrm{t}^m(r,E')\Sigma_\mathrm{f}^m(r,E') \cdot \phi(r,E',\Omega')\mathrm{d}\Omega'\mathrm{d}E'\mathrm{d}\Omega\mathrm{d}E\mathrm{d}r} \tag{3}$$

Ω, E, and r represent the angle, energy, and position, respectively; the superscript m denotes fissile nuclides; i represents the group of delayed neutrons; subscripts d and t represent delayed neutrons and all neutrons, respectively; Φ^* is the adjoint flux; χ is the fission spectrum; u is the number of neutrons produced per fission; Σ_f^m represents the macroscopic fission cross section; Φ is the neutron flux; and v is the neutron speed. The process flow for calculating the kinetic parameters using MagicMC is shown in Fig. 7.

3.1.6 Output module

This module primarily displays the results of data tallied by the tallies module, such as particle flux, reaction rate, dose rate, power distribution, effective multiplication factor, adjoint flux, and kinetic parameters (α, β_{eff}, Λ, ρ). To visually present results in areas of interest to users in a more intuitive way and facilitate the analysis and optimization of geometric structure, material layout, and radiation shielding effects, the MagicMC employs visualization tools from the auxiliary module. This approach addresses the challenge of visualizing multiple radiation fields simultaneously, as the different radiation field data resolutions (mesh sizes) vary by location. Multiple VTK data fields have been developed for these visualization methods [20], as shown in Fig. 8. The visualization processing flow is as follows:

(1) Based on MagicMC, physical field calculations are performed for different tally regions, followed by mesh tallying to obtain multiple fields with mesh data (at various resolutions).

(2) The physical field mesh tally results for each region are processed by extracting spatial topology and field

distribution data, forming a standardized VTK data format.

3.1.7 Auxiliary module

The auxiliary module is designed to enhance the main functionalities and improve the maintainability, user-friendliness, and overall performance of the code-bench. It includes libraries related to the functions of the aforementioned modules, such as mathematical libraries for various probability samplings in source sampling (math), file operation functions, and other functional utilities related to code execution. To enhance stability, this module contains an exception-catching mechanism (Fatal Error, Warning) capable of detecting and handling exceptional situations during the operation of MagicMC, thereby increasing the fault diagnosis capability of the code-bench. Visualization tools are mainly used to display the data results passed from the output module in a 2D/3D format, assisting users in more intuitively understanding the output of the code-bench. The interface information output conveys information to the user, providing the running status, progress reports, date, and the number of running threads, facilitating user interaction with the code-bench.

3.2 Functional unit

Distinct computational and analytical functional modules were developed based on the MagicMC basic unit, integrating variance reduction techniques, activation analysis methods, evolutionary algorithms, and multiphysics coupling methods. These include global variance reduction for shielding analysis, material activation calculations, intelligent shielding optimization, and multiphysics coupling functionalities. Together, these functional modules expand the application scope of MagicMC, meeting the requirements of various types of applications.

3.2.1 Variance reduction functionality

In nuclear reactor physics calculations, especially in large-scale radiation shielding transport calculations, the large-scale and extremely complex structure of reactor geometries can cause the neutron flux rate from the core to the exterior
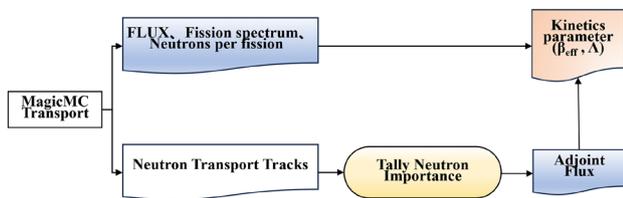

Fig. 7 Process flow of the kinetic parameter tally method
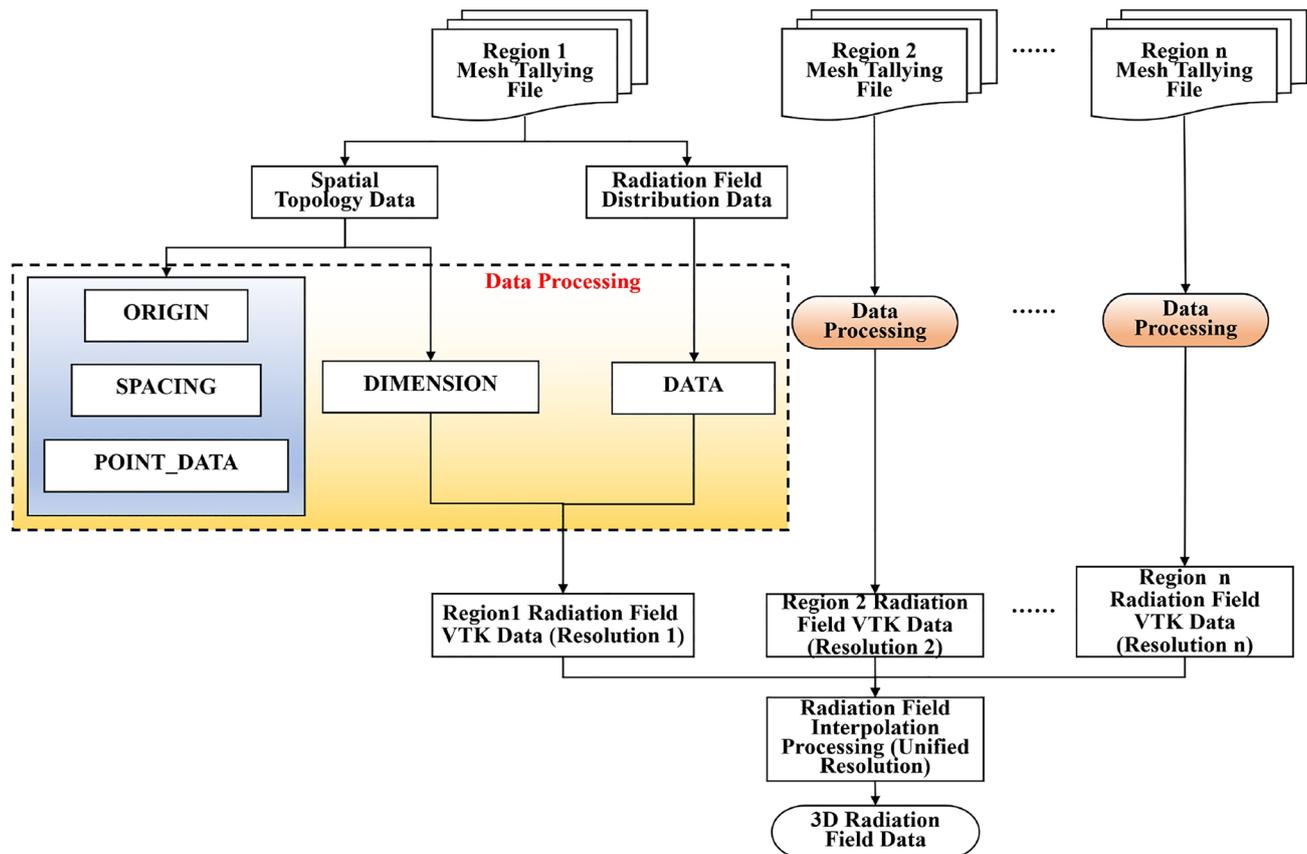
Fig. 8 Data visualization method with multiple VTK format fields

to vary significantly–sometimes by more than ten orders of magnitude. When using the Monte Carlo method, this often leads to issues such as low-probability deep penetration problems, high computational resource demands, and convergence difficulties. MagicMC has developed a mesh-based weight window module to address large-scale deep penetration challenges [21]. The global variance reduction (GVR) technique, based on the MC anti-forward transport method, was derived from the weight window lower limit bias parameter generation method of MC anti-forward transport. Unlike other variance reduction methods (e.g., CADIS), this technique does not require consideration of code coupling and mesh mapping. Figure 9 shows the computational flow of the global variance reduction technique based on MC anti-forward transport in MagicMC [22].

The adaptive global variance reduction method is illustrated in Fig. 10. Based on the model data provided by the user, a particle transport simulation is conducted to obtain the forward flux. Using the simulation results, data processing is performed with Formula (4), introducing a smoothing factor SI ($SI \in [0, 1]$) to generate importance weight windows. The smoothing factor SI is used to prevent excessive particle splitting due to large gradients in the lower parameter of the weight window. Typically, the SI value defaults to 1.0. However, when

the majority of the simulated geometry is shielded, SI can be set to 0.5–1.0, and when only the far-source region of the simulated geometry is shielded, the SI value can be set between 0.0–0.5. These values for SI were obtained through empirical test calculations. The generated weight window is then used to update the input file for the next generation, and the number of particles is doubled from the previous generation. Following this concept, each generation is iterated in the same manner. Users can select the number of iterations and the initial particle count for the first generation. This functionality also allows for continued computation if system errors occur or if initial particle counts yield insufficient results, ensuring the accuracy of the calculations.

$$
w_{th}(r) = \left(\frac{\phi(r)}{\phi(\max)} \right)^{SI}
\tag{4}
$$

Here, $w_{th}(r)$ represents the lower limit of the weight window in space r, $\Phi(r)$ is the flux rate in space r, Φ_{max} represents the maximum flux for the entire model, and SI is the smoothing factor with variable values.
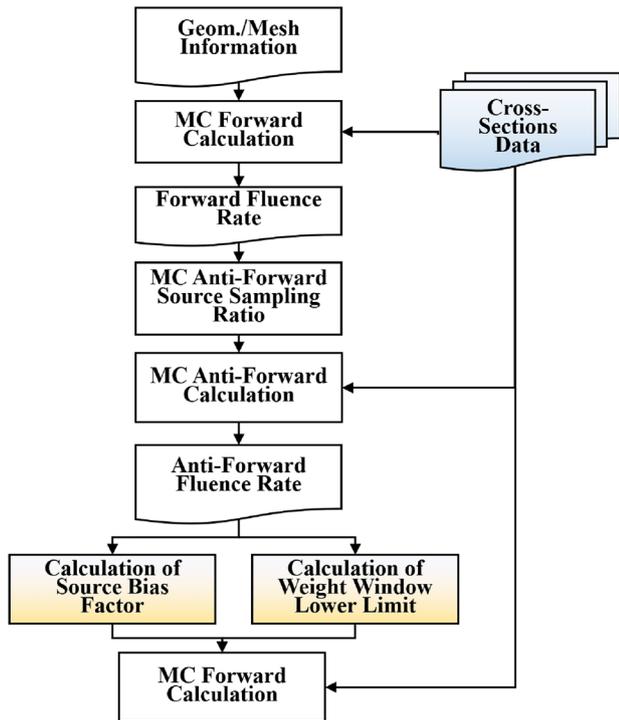
Fig. 9 Global variance reduction method based on anti-forward flux

3.2.2 High-resolution activation functionality

During nuclear reactor operation, neutron activation reactions lead to the production of a large number of radioactive nuclides within the reactor's structural materials. This

directly impacts radiation safety considerations, including reactor shielding design, maintenance planning, refueling strategies, and decommissioning plans-crucial aspects of reactor design [23–26]. Conventional activation methods, typically cell-based, do not consider the spatial distribution of neutron flux within a cell and thus cannot accurately describe the nonuniform spatial effects of activation in structural materials. This limitation can lead to coarse distributions of source terms and decay γ-source, thereby limiting the precise evaluation of the radiation dose induced by decay γ-source. To address these issues, this study developed a mesh-based high-resolution activation module for reactor structural materials using the Rigorous-2-Step (R2S) method, as shown in Fig. 11. This process includes three main steps: neutron transport, mesh-based activation, and decay photon dose calculations.

(1) *Neutron transport calculations*: A Monte Carlo model of reactor structural materials is established for neutron transport calculations. Mesh tally models are created for structural material components. Based on MagicMC, Monte Carlo neutron transport calculations are performed to obtain mesh-based neutron flux and reaction rates for structural material regions.

(2) *Mesh-based activation calculation*: For structural material components, a mesh model is created for activation calculations. Mesh activation calculations are performed using mesh-based neutron flux and reaction rates from neutron transport calculations. This provides a high-resolution distribution of mesh-based activation source terms, including mesh decay photon source

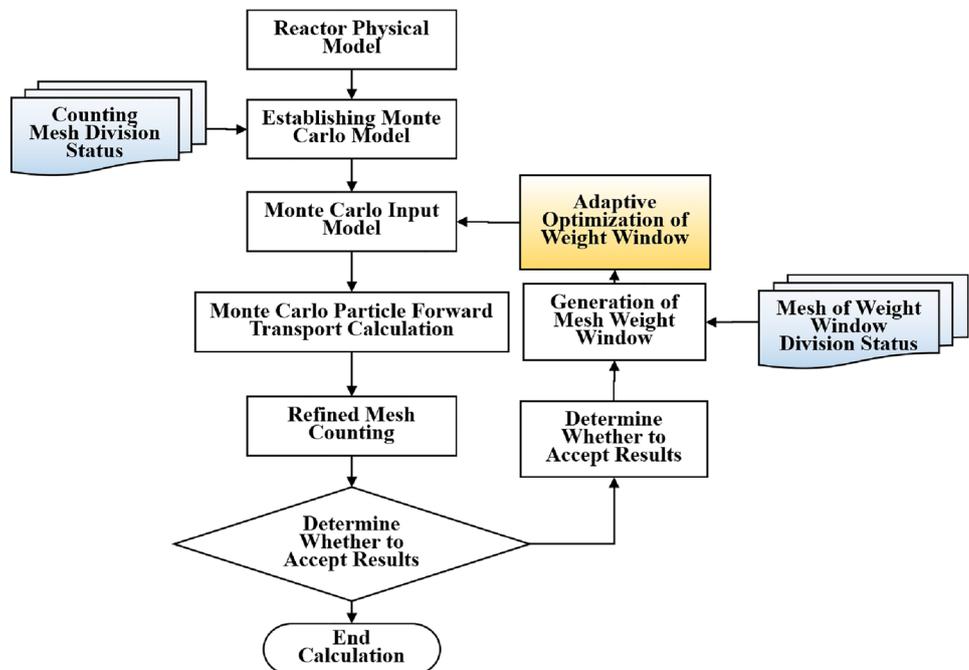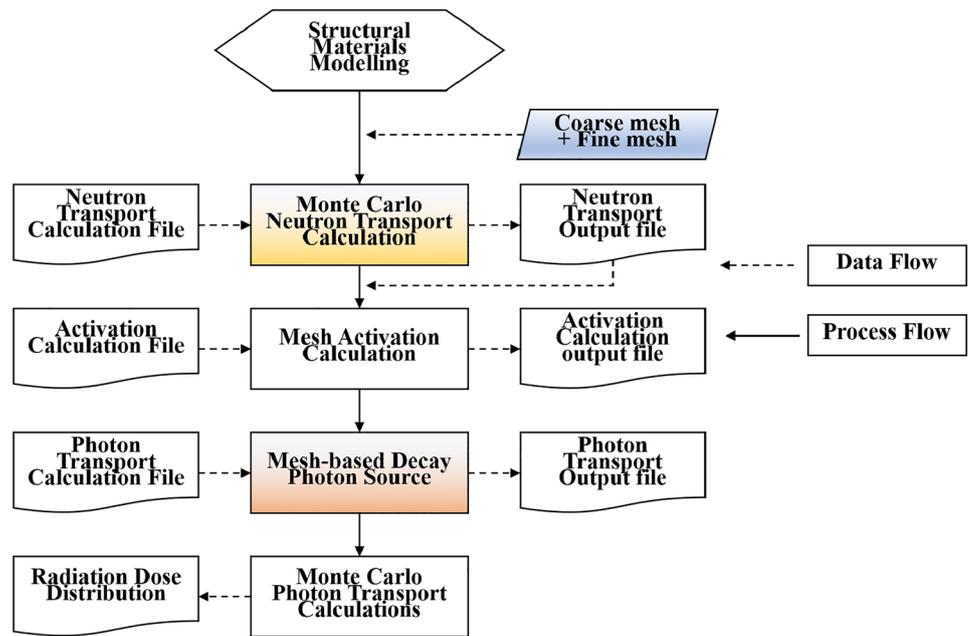**Fig. 10** Adaptive global variance reduction method based on forward flux

strength, decay photon energy spectrum, and the main activated nuclides.

(3) *Decay photon dose calculation*: Using the mesh-based decay photon source derived from mesh-based activation calculations, a mesh-based source sampling method is integrated into MagicMC. A Monte Carlo photon transport calculation is then performed with the mesh-based decay photon source, and the radiation dose rates induced by the decay photon source are obtained through mesh tallying.

3.2.3 Shielding intelligent optimization functionality

Reactor radiation shielding design is a typical multi-objective optimization problem, requiring comprehensive consideration of factors such as weight, volume, and radiation dose rates to achieve an optimal design solution [27–36]. Traditional design methods heavily rely on expert experience and are limited by low efficiency, high uncertainty, and suboptimal solutions, making them unsuitable for rapid design processes. The shielding optimization module in MagicMC includes built-in algorithm interfaces, enabling the automated invocation of multi-objective optimization algorithms, such as NSGA-II, NSGA-III, and MOPSO. This facilitates the iterative optimization of shielding schemes, thereby optimizing the design of shielding structures and materials. The main steps of the shielding intelligent optimization module are as follows:

(1) *Pre-processing*: Acquiring user-specified structures or regions for optimization, defining optimization objectives (e.g., weight, volume, and dose), constraint parameters, etc.

(2) *Optimization simulation*: Utilizing evolutionary algorithms for automated radiation shielding encoding and selecting appropriate algorithms for optimization design. Through the algorithm interface, data transmission between the MagicMC transport calculation and optimization algorithms is completed, iteratively obtaining the optimal solution set.

(3) *Post-processing*: Recommending design solutions based on evaluation indicators and visually presenting the optimization results.

The shielding optimization module leverages the advantages of various optimization algorithms, effectively balancing multiple design objectives and rapidly determining the optimal parameters for reactor shielding design, including shielding thickness, structural layout, and material composition. Within the defined constraints, it achieves optimization objectives related to minimizing shielding structure volume, space occupation, and protection costs. This module provides valuable guidance for novel reactor shielding designs. The shielding optimization module is illustrated in Fig. 12.

3.2.4 Multiphysics coupling functionality

The normal operation of a nuclear reactor involves the coupling of multiple physical fields, spanning disciplines such as neutronics, heat transfer, fluid dynamics, and structural mechanics [37–39]. In transient-oriented neutronics and thermal-hydraulics coupling problems, MagicMC can provide time-dependent calculations of reactor power and its
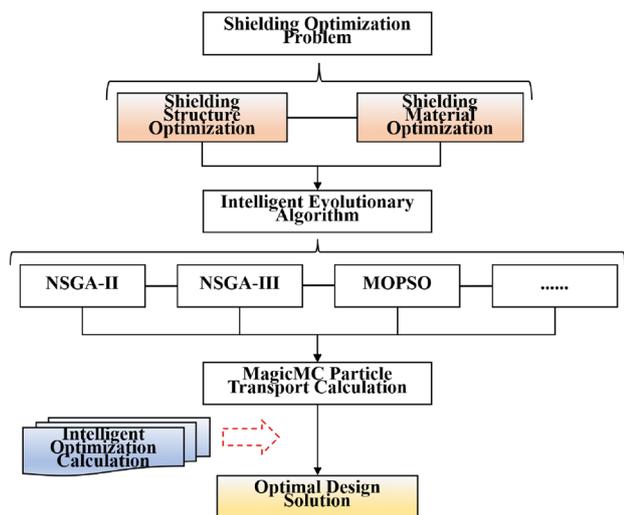
Fig. 12 Shielding optimization functionality with evolutionary algorithms
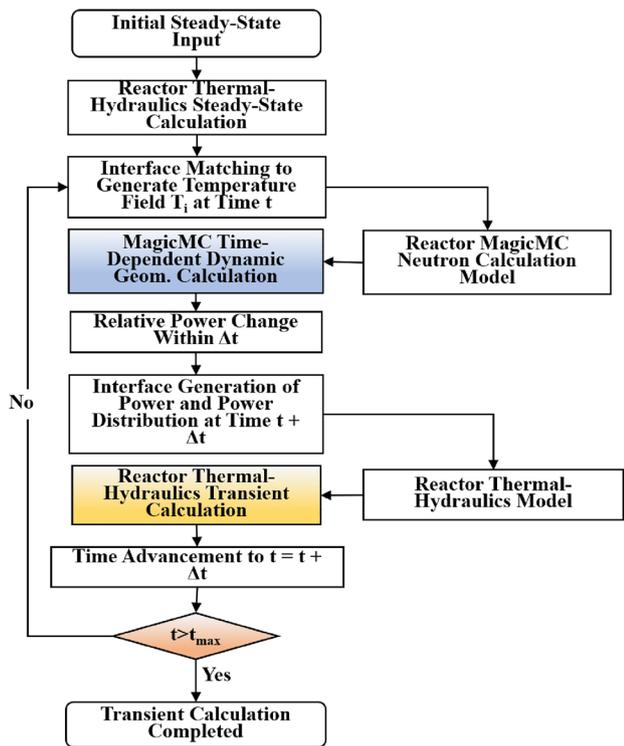

Fig. 13 Transient neutronics and thermal-hydraulics coupling method

distribution changes. Using neutronics data, users can perform transient thermal calculations to determine the temperature field of a reactor at different times. MagicMC generates temperature-dependent cross sections online through a mapping relationship. This process calculates the impact of thermal feedback on reactor operation, achieving transient neutronics and thermal-hydraulics coupling. The transient

neutronics and thermal-hydraulics coupling based on MagicMC is illustrated in Fig. 13.

Monte Carlo codes require substantial computational resources for time-dependent calculations, particularly for long-duration transient processes. This demand, coupled with the need to perform calculations across multiple physical fields, makes the simulation computation time a critical limiting factor. MagicMC includes a module for calculating the average reactor temperature coefficient as part of neutronics-thermal-mechanical coupling calculations for reactors, building on online temperature-dependent cross-sectional processing. This module uses the point kinetics method to evaluate changes in reactor power and power distribution. Integration with ANSYS for finite-element thermal stress calculations yields results such as reactor temperature fields, structural displacements, and stresses. These results are then fed back to both MagicMC and the point kinetics code, completing the neutronics-thermal-mechanical coupling calculations for the reactor [40]. The process is illustrated in Fig. 14.

4 Numerical simulations with MagicMC for nuclear applications

To validate the reliability of MagicMC, various international benchmarks and numerical models were employed in the numerical simulations, including transient analysis, shielding optimization, activation calculation, shielding calculations, and dosimetry calculations. The simulation results were compared to experimental data or reference solutions.

4.1 Transient simulation for TRIGA reactor

Due to the characteristics of the TRIGA reactor, such as significant power changes and short pulse durations, performing transient simulations of the TRIGA reactor using the Monte Carlo method has been a longstanding challenge. To meet the computational requirements for the TRIGA reactor, MagicMC developed functionalities for dynamic geometry tracking and time-dependent Monte Carlo calculations, allowing for a physical description of the reactor's control rod movements during transients. Additionally, the on-the-fly temperature cross-section generation functionality in MagicMC captures thermal feedback during rapid power changes. By leveraging its multiphysics coupling functionality, MagicMC achieved a transient simulation of a TRIGA reactor using the pure Monte Carlo method. The JSI TRIGA Mark II reactor was chosen as the benchmark [41], with the reactivity insertion set at 2. The power curve based on physical-thermal coupling, using both MagicMC
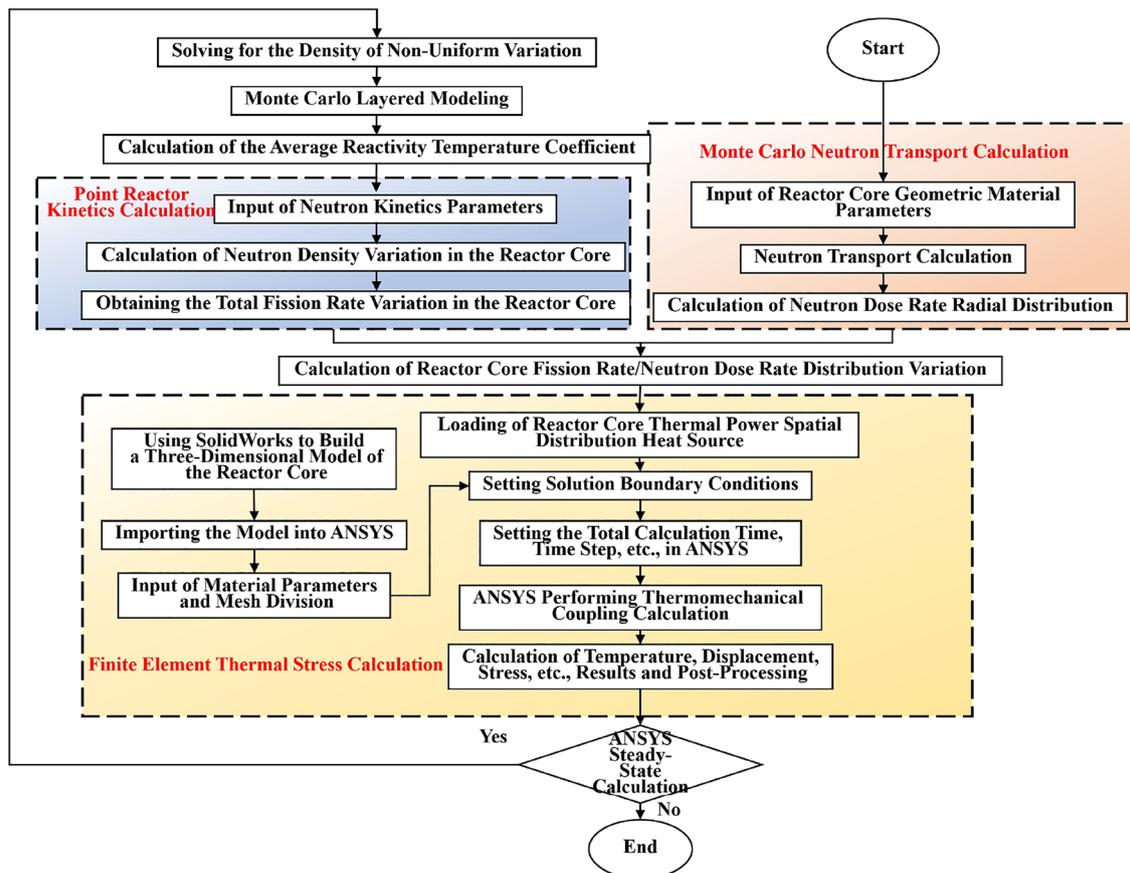
Fig. 14 Multiphysics coupling of the neutronics-thermal-mechanical coupling method

and a subchannel program, is shown in Fig. 15. The simulation yielded a peak power of 224.1 MW, an integral energy of 6.83 MWs, and a peak power full-width at half maximum (FWHM) of 27.27 ms, which compare consistently with the experimental values of 222.6 MW peak power and 6.83 MWs integral energy from the official documentation of the JSI TRIGA Mark II reactor.

4.2 Multi-objective optimization for shielding design

To address the problem of multi-objective and multi-parameter optimal design for reactor radiation shielding, multi-objective optimization for shielding design was conducted using the shielding optimization functionality in MagicMC. By leveraging its shielding optimization capabilities, a third-generation nondominated genetic algorithm (NSGA-III) was coupled with MagicMC to optimize both a simple 3D shielding structure (Fig. 16a) and a complex 3D shielding structure (Fig. 16b). Numerical results were then compared with those obtained using the reference algorithm, NSGA-II.

For the simple 3D shielding structure, the optimization objectives were the total weight, total volume of the shielding layer, and normalized dose rates axially below and radially to the side of the shielding layer. The optimization parameters were set as follows: population size of 210, 100 genetic generations, single-layer thickness ranging from 0.25 cm to 13 cm, and mutation probability between 0.01 and 0.05 for iterative optimization. The mean values of the objectives in the final generation are shown in Fig. 17. As shown, MagicMC combined with NSGA-III outperformed the traditional algorithm NSGA-II for each mutation probability.

For the complex 3D shielding structures, the optimization objectives included the total volume and total weight of the R1-R8 and U1-U3 shielding layers, as well as the dose rates radially and axially superior to the shielding layers. Variable parameters included shield thickness, shield material, and material composition. The parameters were set with a population size of 100, 50 genetic generations, and single-layer thicknesses between 15 and 80 cm. The optimized ratios for various objectives in the final generation are shown in Fig. 18. Results indicate that, compared with the traditional
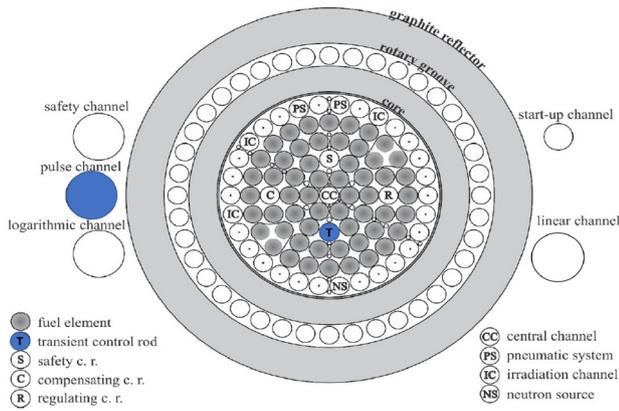
(a)
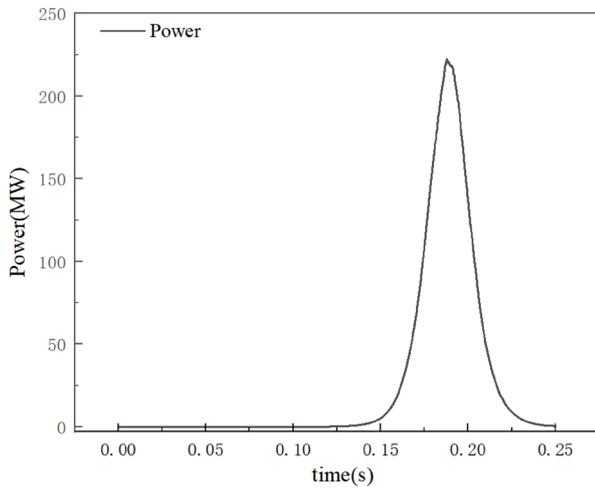
(b)

Fig. 15 Schematic of the TRIGA Mark II reactor and pulse power variation with the injection of 2\$ reactivity. **a** Geometry model of the JSI TRIGA Mark II reactor; **b** The time-dependent power distribution

optimization algorithm NSGA-II, the outcomes using MagicMC were superior.

4.3 High-resolution material activation analysis

To address the precise activation analysis of reactor structural materials with complex configurations and varied material arrangements, a mesh-based, high-resolution activation analysis method for reactor structural materials has been developed based on MagicMC. This approach includes a transport-activation-dosimetry automatic coupling interface, enabling precise activation analysis of reactor structural materials and accurate evaluation of the radiation dose field induced by decay photons. This provides theoretical and technical support for ensuring radiation safety during nuclear facility maintenance and
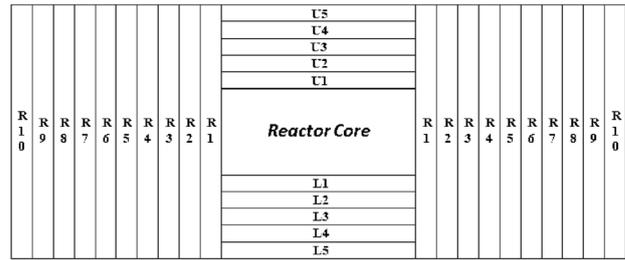
(a)
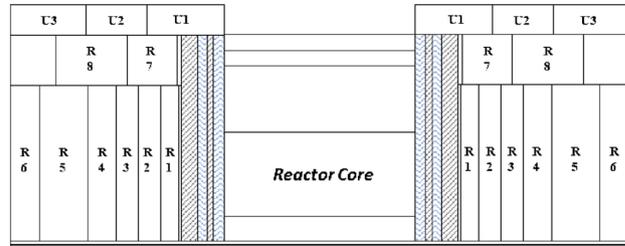
(b)

Fig. 16 Reactor shielding structures for two numerical models. **a** Simple 3D shielding structure; **b** Complex 3D shielding structure

decommissioning. In this study, a mesh-based activation analysis was conducted on a VVER pressurized water reactor [42–44]. The VVER reactor core comprises 163 hexagonal assemblies, each containing 331 rods, including 311 fuel rods, a central tube, a neutron-measuring tube, and 18 guide tubes. The core's equivalent diameter and height are 316 cm and 353 cm, respectively. The reactor's external structure includes the core barrel, core basket, and pressure vessel. A geometric model of the VVER reactor is shown in Fig. 19.

The modeled structure for activation in the VVER pressurized water reactor includes the pressure vessel, subjected to an irradiation duration of one year and a cooling period of 30 days. Using MagicMC, the decay photon source strength of the pressure vessel was calculated, as shown in Fig. 20. MagicMC utilizes cylindrical meshes to perform this mesh-based activation analysis, with the model divided into 16 and 32 meshes in the angular and axial directions, respectively. The results indicate that regions with higher decay photon source strengths in the angular direction align with the positions of the corner assemblies, where core components are closer to the pressure vessel.

4.4 High-fidelity radiation shielding calculations

The 3D RADIATION TRANSPORT BENCHMARK problem [45] was employed to verify the MC anti-forward global variance reduction method developed in MagicMC. The benchmark has dimensions of 100 cm × 100 cm × 100 cm,
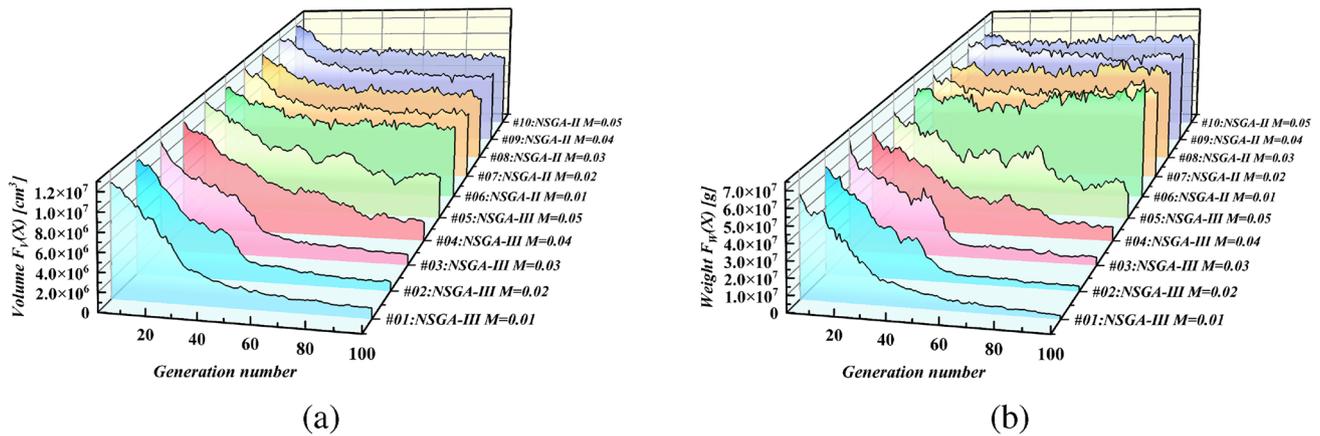
Fig. 17 (Color online) Plot of changes in mean values of objectives for simple 3D shielding structures. **a** Mean values of total volume for shielding system with various mutation probabilities; **b** Mean values of total weight for shielding system with various mutation probabilities
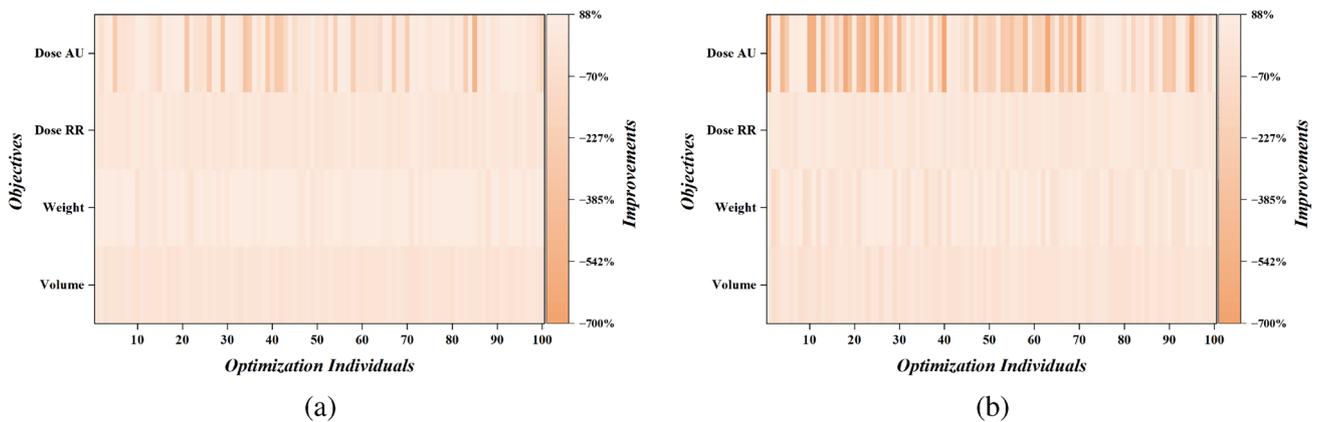

Fig. 18 (Color online) The optimized ratio heat map for complex 3D shielding structures. **a** Optimized ratio heatmap with NSGA-III and **b** optimized ratio heatmap with NSGA-II
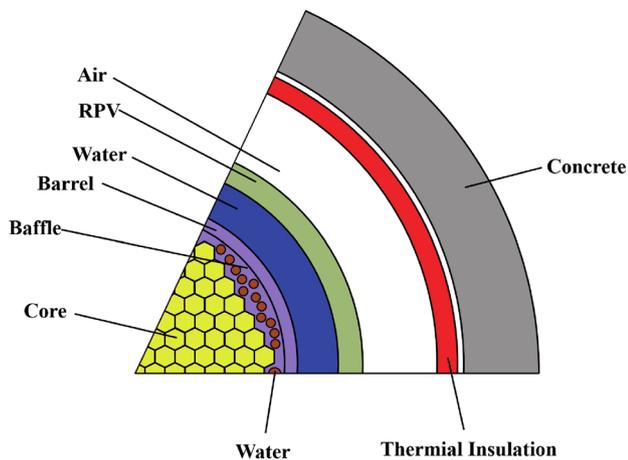

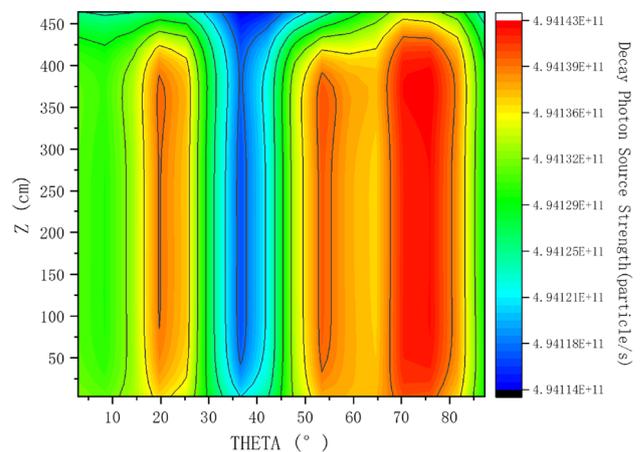**Fig. 19** (Color online) Horizontal cross-section view of the VVER reactor

Fig. 20 (Color online) High-resolution distribution of decay photon source strength in the VVER pressure vessel
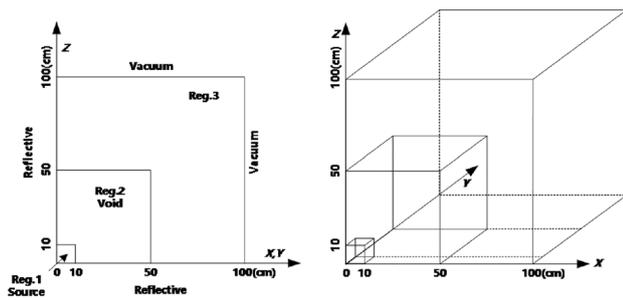
Fig. 21 3D radiation shielding benchmark model

with a source region of (10 cm × 10 cm × 10 cm), as illustrated in Fig. 21.

By setting the transported particle count to (1×10^5) for both the direct simulation and the simulation using the global variance reduction method with anti-forward flux, the results are shown in Figs. 22 and 23. In Fig. 22, the direct simulation shows a deep penetration problem on the plane at $(Z = 70\,\text{cm})$, with the issue becoming more pronounced as (Z) increases, accompanied by a rise in the rate of zero-flux meshes. However, as seen in the figure, using the weight window constructed based on anti-forward flux results in a proportion of errors below 20% on the $(Z = 70\,\text{cm})$ plane, which remained above 80%, validating the accuracy of the lower limit setting in the weight window. In Fig. 23, on

the planes at $(Z = 10\,\text{cm})$ and $(Z = 30\,\text{cm})$, errors on the $(Z = 10\,\text{cm})$ plane are greater than those on the $(Z = 50\,\text{cm})$ plane. This discrepancy stems from a point detector placed at the vertex of the $(Z = 50\,\text{cm})$ plane, but absent from the $(Z = 30\,\text{cm})$ plane. Consequently, a higher-quality weight window near the vertex of the $(Z = 30\,\text{cm})$ plane was achieved compared to the $(Z = 10\,\text{cm})$ plane.

By analyzing the mesh flux across the entire model, the results shown in Table 1 and Fig. 24 were obtained. Compared with direct simulation, using the anti-forward flux variance reduction method in MagicMC decreased the zero-flux mesh rate from 13.09% to 0.00%. Additionally, the average relative error was reduced from 59.38% to 24.43%, the proportion of meshes with a relative error below 20% increased from 1.11% to 44.75%, and the proportion of meshes with an error below 50% increased from 46.33% to 95.19%. These statistical results indicate that, compared to direct simulation, the global variance reduction method based on anti-forward flux improves the accuracy of deep penetration problems and enhances particle transport simulation efficiency.

4.5 Medical dosimetry calculation for BNCT

Boron neutron capture therapy (BNCT) is often regarded as the "atomic bomb" of twenty-first-century cancer treatment, offering a highly effective binary-targeted radiotherapy approach. Dose calculation is fundamental and crucial for the BNCT treatment planning system (TPS).
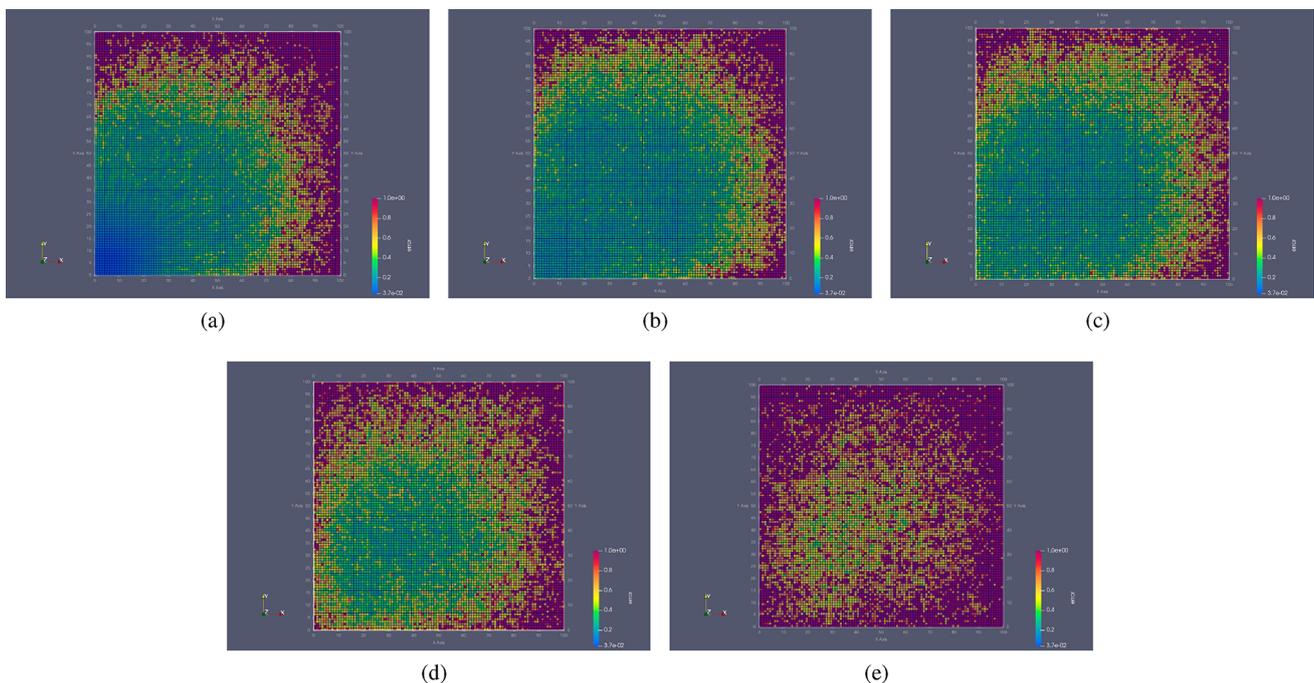

(a)   (b)   (c)

(d)   (e)

Fig. 22 (Color online) Relative errors distribution with direct MC simulation. **a** $Z = 10\,\text{cm}$, **b** $Z = 30\,\text{cm}$, **c** $Z = 50\,\text{cm}$, **d** $Z = 70\,\text{cm}$, **e** $Z = 90\,\text{cm}$
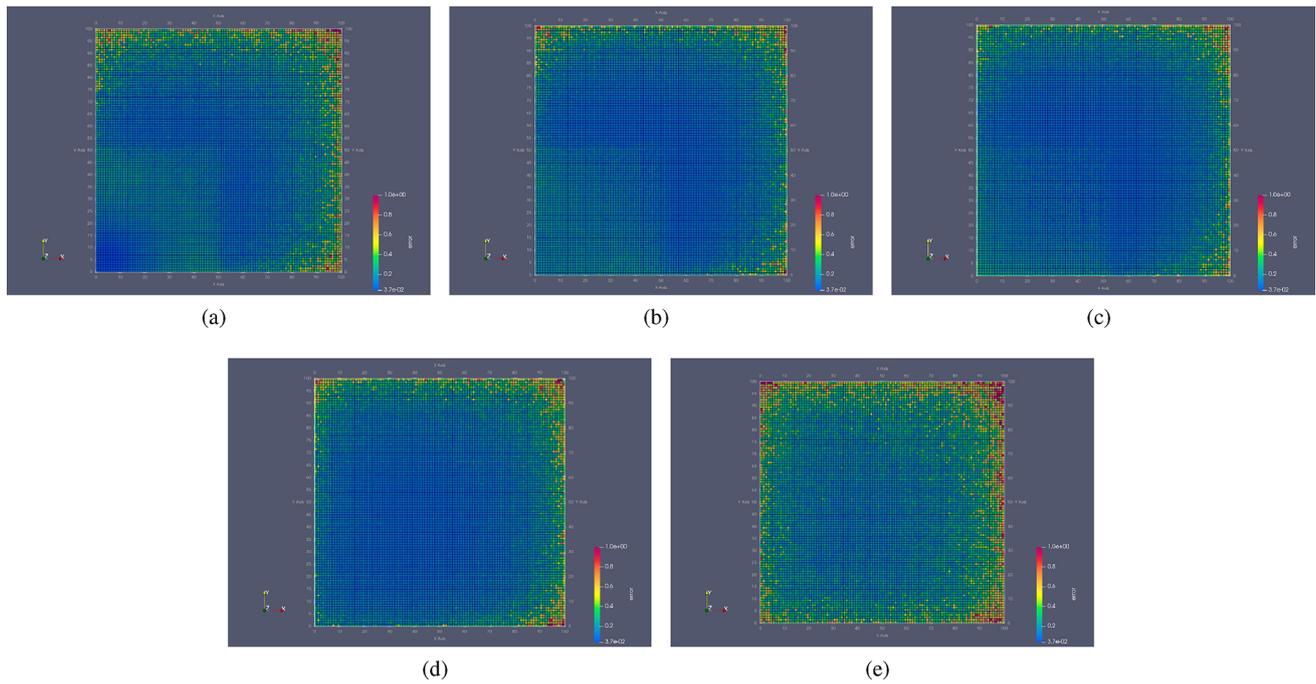
Fig. 23 (Color online) Relative errors distribution with GVR MC simulation. **a** $Z = 10$ cm, **b** $Z = 30$ cm, **c** $Z = 50$ cm, **d** $Z = 70$ cm, **e** $Z = 90$ cm

Table 1 Statistical results of the direct and global variance reduction simulations

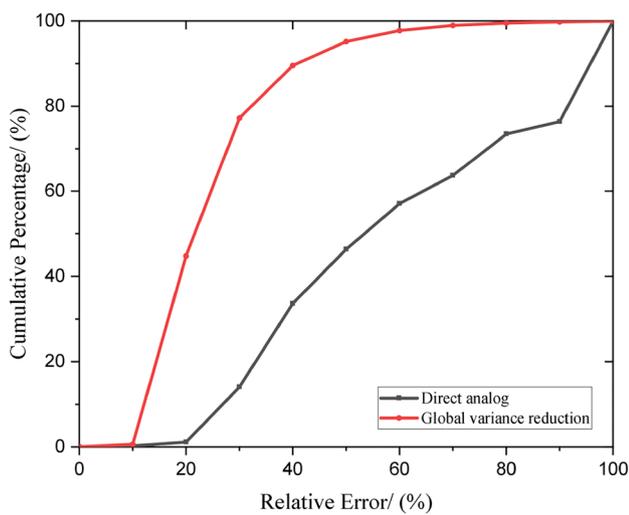| Simulation method	Average relative error (%)	Zero-flux mesh rate (%)	Proportion of meshes with relative error below 20% (%)	Proportion of meshes with relative error below 50% (%)
Direct simulation	59.38	13.09	1.11	46.33
Global variance reduction simulation	24.43	0.00	44.75	95.19

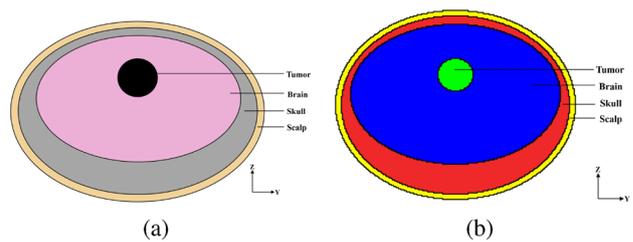**Fig. 24** Cumulative distribution of relative errors

Fig. 25 (Color online) Cross-section view of the Snyder model. **a** Analytical model and **b** 1 mm-level voxel model (MagicMC)

Using MagicMC, the international Snyder model benchmark was analyzed in this study, as shown in Fig. 25. A 1 mm-resolution voxel model was constructed to closely approximate the analytical model, with voxel model materials populated using the mesh center point method. MagicMC was employed to simulate the depth-dose rate curve, and the results were compared to reference solutions. Since
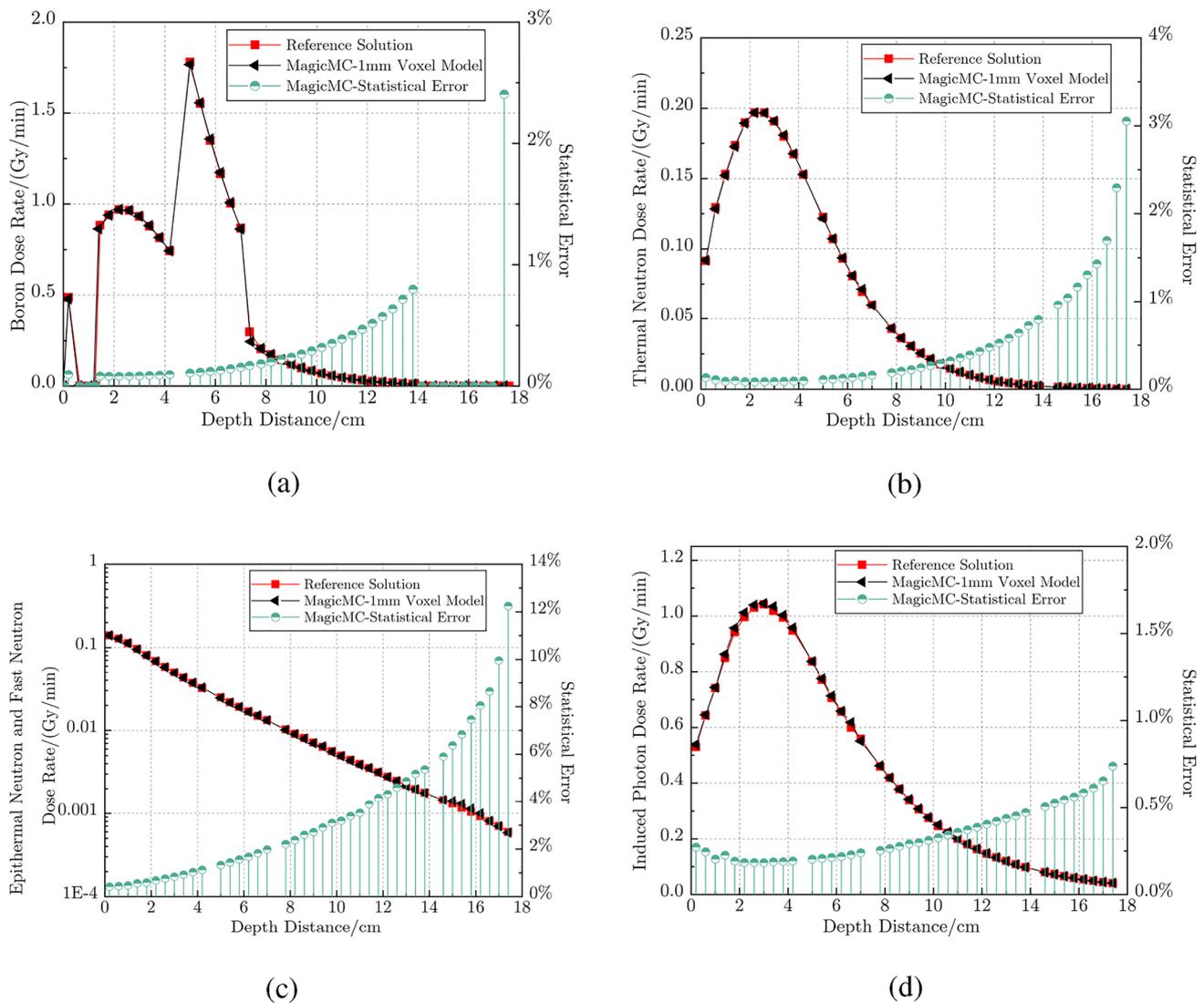
(a)

(b)

(c)

(d)

Fig. 26 Comparison of depth-dose rate distribution curves. **a** Depth-boron dose rate distribution curve and statistical error, **b** depth-thermal neutron dose rate distribution curve and statistical error, **c** depth-epithermal and fast neutron dose rate distribution curve and statistical error, **d** depth-induced photon dose rate distribution curves and statistical error

the MCNP program is often considered the "gold standard" for Monte Carlo calculations and widely used for validating other Monte Carlo programs, MCNP was used here to simulate the Snyder model dose rate. These MCNP results served as reference solutions to verify the accuracy of dose calculations performed by MagicMC [46].

To mitigate the deep penetration issues inherent in Monte Carlo simulations, MagicMC conducted a particle transport simulation with 1×10^8 particles to ensure adequate sampling. Figure 26 presents the distribution curves of the boron dose rate, thermal neutron dose rate, epithermal and fast neutron dose rates, induced photon dose rate as a function of depth, and the statistical errors in the MagicMC calculations.

From the numerical simulation results, it can be observed that MagicMC's statistical error gradually increases with depth, especially in Fig. 26c, where the large statistical error beyond 12 cm depth is primarily due to the deep penetration challenge in Monte Carlo simulations, resulting in reduced sampling of epithermal neutrons at greater depths. Overall, the distribution curves for boron dose rate, thermal neutron dose rate, epithermal and fast neutron dose rates, and secondary photon dose rate calculated with MagicMC align closely with the reference solutions, confirming the accuracy of MagicMC for BNCT radiotherapy applications.

Since boron concentration in BNCT varies post-injection in the human body, BNCT dose calculations can be conducted rapidly. To assess MagicMC's efficiency in
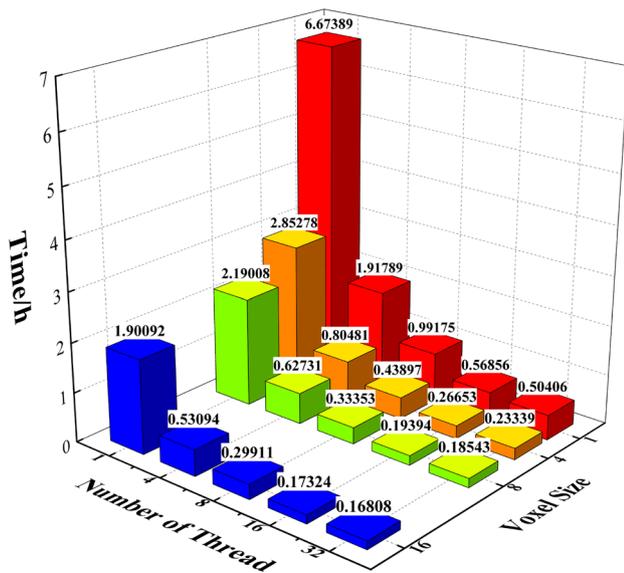
Fig. 27 (Color online) Comparison of computation time (*h*) for different voxels scales and different number of threads 3D histograms

Table 2 The number of meshes for each voxel model

Voxel size (mm)	Number of voxels
16	2744
8	21952
4	175616
1	11239424

BNCT calculations, this simulation was executed on an Intel(R) Xeon(R) Silver 4210R CPU @ 2.40GHz, with parameters simulated using 1, 4, 8, 16, and 32 threads for the Snyder head voxel model, with voxel sizes of 16 mm, 8 mm, 4 mm, and 1 mm. The number of meshes for each voxel model is shown in Table 2.

The computational efficiency of using 1, 4, 8, 16, and 32 threads was evaluated for different mesh scales by running MagicMC simulations on a 1×10^8 particle history. The 3D histogram in Fig. 27 shows the computational time (h) for various voxel sizes of the Snyder model in relation to different thread counts.

As illustrated in the figure, for a given set of computational conditions, smaller voxel sizes result in longer simulation times. However, increasing the number of parallel threads significantly reduces the computation time, with a more pronounced acceleration effect as thread count rises.

5 Conclusion

This study presents the development of MagicMC, a new Monte Carlo-based code designed as a high-fidelity, high-resolution, and highly adaptable tool for complex nuclear applications. The architecture, core modules, functional components, associated methods, and algorithms have been detailed. Numerical results demonstrate the efficiency, accuracy, and reliability of MagicMC in preliminary applications. MagicMC serves not only as a Monte Carlo particle transport code but also as a flexible platform integrating specialized functionalities for dedicated applications, including radiation shielding optimization, high-resolution material activation, multi-physics coupling, and medical dosimetry. The overarching goal of MagicMC is to evolve into an intelligent tool for nuclear applications through the incorporation of increasingly advanced methods. Currently, MagicMC is in its initial development phase, yet it shows substantial potential for various nuclear applications. Future work will prioritize algorithm optimization and enhanced intelligent computing capabilities to address increasingly complex and varied applications. This can provide crucial technical support for breakthroughs in high-fidelity, high-resolution, and intelligent Monte Carlo-based design tools tailored to advanced nuclear applications.

Declarations

Conflict of interest The authors declare that they have no Conflict of interest.

References

1. B.L. Sjenitzer, J.E. Hoogenboom, A Monte Carlo method for calculation of the dynamic behaviour of nuclear reactors. Prog. Nucl. Sci. Technol. **2**, 716–721 (2011). https://doi.org/10.15669/pnst.2.716

2. R.Y. Rubinstein, D.P. Kroese, *Simulation and the Monte Carlo Method* (John Wiley & Sons, Hoboken, 2016). https://doi.org/10.1002/9781118631980

3. W.L. Dunn, J.K. Shultis, *Exploring Monte Carlo Methods* (Elsevier, Amsterdam, 2022)

4. J.A. Kulesza, T.R. Adams, J.C. Armstrong et al., *MCNP®Code Version 6.3.0 Theory & User Manual* (Los Alamos National Lab, 2022)

5. P.K. Romano, N.E. Horelik, B.R. Herman et al., OpenMC: a state-of-the-art Monte Carlo code for research and development. Ann. Nucl. Energy **82**, 90–97 (2015). https://doi.org/10.1016/j.anucene.2014.07.048

6. S. Agostinelli, J. Allison, K. Amako et al., GEANT4-a simulation toolkit. Nucl. Instrum. Meth. Phys. Res. Sect. A **506**, 250–303 (2003). https://doi.org/10.1016/S0168-9002(03)01368-8

7. A. Ferrari, P. Sala, A. Fasso et al., Fluka: a multi-particle transport code. Tech. Rep. (2005). https://doi.org/10.2172/877507

8. K. Wang, Z.G. Li, D. She et al., RMC-a Monte Carlo code for reactor core analysis. Ann. Nucl. Energy **82**, 121–129 (2015). https://doi.org/10.1016/j.anucene.2014.08.048

9. C. Yang, T. Cheng, L. Deng et al., Development of 3-D parallel first-collision source method for discrete ordinate code JSNT-S. Ann. Nucl. Energy **135**, 106942 (2020). https://doi.org/10.1016/j.anucene.2019.106942

10. Y.C. Wu, J. Song, L.Q. Hu, Super Monte Carlo simulation program for nuclear and radiation process: SuperMC. Chinese Journal of Nuclear Science and Engineering **36**, 62–71 (2016). (**in Chinese**)

11. Z.P. Chen, J.S. Xie, Q. Guo et al., Physics-oriented optimization strategy for the energy lookup algorithm in continuous energy Monte Carlo neutron transport simulation. Comput. Phys. Commun. **234**, 146–158 (2019). https://doi.org/10.1016/j.cpc.2018.07.016

12. R.L. Harrison, Introduction to Monte Carlo simulation. AIP Conf. Proc. **1204**, 17–21 (2010). https://doi.org/10.1063/1.3295638

13. F.Y. Xu, C. Yang, T. Yu et al., Research on automatic modeling method of TORT program based on CAD model. Nucl. Power Eng. **44**, 49–54 (2023). https://doi.org/10.13832/j.jnpe.2023.04.0049. (**in Chinese**)

14. Y.C. Wu, J. Song, H.Q. Zheng et al., CAD-based Monte Carlo program for integrated simulation of nuclear system SuperMC. Ann. Nucl. Energy **82**, 161–168 (2015). https://doi.org/10.1016/j.anucene.2014.08.058

15. M.A. Wasaye, H. Wang, H. Zheng et al., The hybrid model for sampling multiple elastic scattering angular deflections based on Goudsmit–Saunderson theory. Nucl. Technol. Radiat. Prot. **32**, 229–235 (2017). https://doi.org/10.2298/NTRP1703229W

16. M.A. Wasaye, H. Wang, P. He, An algorithm for Monte Carlo simulation of bremsstrahlung emission by electrons. Nucl. Sci. Tech. **28**, 71 (2017). https://doi.org/10.1007/s41365-017-0218-7

17. M.A. Wasaye, T. Yu, J.S. Xie et al., A fast sampling algorithm for energy-angle distributions of bremsstrahlung photon for radiotherapy applications. J. Korean Phys. Soc. **82**, 954–962 (2023). https://doi.org/10.1007/s40042-023-00750-9

18. X. Zhang, S.C. Liu, Y.X. Chen, Development of Monte Carlo hybrid parallel algorithm and application in high resolution spatial-energy flux distribution calculation. Nucl. Eng. Des. **413**, 112500 (2023). https://doi.org/10.1016/j.nucengdes.2023.112500

19. K.K. Gao, Z.P. Chen, A.K. Sun et al., Development and verification of the GPU-based Monte Carlo particle transport program MagiC. In *Proceedings of IEEE IAECST* pp. 194–199 (2024). https://doi.org/10.1109/IAECST60924.2023.10503564

20. L.J. Kuang, T. Yu, H.J. Zhang et al., CAD-based inversion visualization of Monte Carlo computational model based on SALOME. High Power Laser Part. Beams **35**, 036001 (2023). https://doi.org/10.11884/HPLPB202335.220276. (**in Chinese**)

21. X. Zhang, S. Liu, J. Zhang et al., Development and application of variance reduction technique based on response matrix method in the cosRMC code. Ann. Nucl. Energy **186**, 109753 (2023). https://doi.org/10.1016/j.anucene.2023.109753

22. A.K. Sun, Z.P. Chen, L.M. Li et al., Research on shielding deep penetration calculation based on MC variance reduction techniques. PBNC, 285 (Springer, Singapore, 2023). https://doi.org/10.1007/978-981-19-8899-8_79

23. X.D. Yuan, H.Q. Ma, Z.P. Chen et al., Study on activation-induced dose calculation of reactor structural materials. Nucl. Power Eng. **42**, 103–109 (2021). https://doi.org/10.13832/j.jnpe.2021.05.0103. (**in Chinese**)

24. L.M. Li, S.Y. Jiang, Z.P. Chen et al., Mesh-based activation analysis for structural materials in nuclear reactor. Nuclear Techniques (in Chinese) **45**, 080601 (2022). https://doi.org/10.11889/j.0253-3219.2022.hjs.45.080601

25. A. Davis, R. Pampin, Benchmarking the MCR2S system for high-resolution activation dose analysis in ITER. Fusion Eng. Des. **85**, 87–92 (2010). https://doi.org/10.1016/j.fusengdes.2009.07.002

26. S. Wang, S. Liu, J. Wu et al., Analysis of transport-activation internal coupling method implemented in Monte Carlo code cosRMC. Fusion Eng. Des. **202**, 114395 (2024). https://doi.org/10.1016/j.fusengdes.2024.114395

27. J.C. Lei, C. Yang, H.J. Zhang et al., Radiation shielding optimization design research based on bare-bones particle swarm optimization algorithm. Nucl. Eng. Technol. **55**, 2215–2221 (2023). https://doi.org/10.1016/j.net.2023.02.018

28. Z.P. Chen, Z.Y. Zhang, J.S. Xie et al., Multi-objective optimization strategies for radiation shielding design with genetic algorithm. Comput. Phys. Commun. **260**, 107267 (2021). https://doi.org/10.1016/j.cpc.2020.107267

29. Z.P. Chen, Z.Y. Zhang, J.S. Xie et al., Metaheuristic optimization method for compact reactor radiation shielding design based on genetic algorithm. Ann. Nucl. Energy **134**, 318–329 (2019). https://doi.org/10.1016/j.anucene.2019.06.031

30. Q.F. Cao, Z.Y. Zhang, Z.P. Chen et al., Study on multi-objective optimization method for radiation shielding based on non-dominated sorting genetic algorithm. Nucl. Power Eng. **41**, 167–171 (2020). https://doi.org/10.13832/j.jnpe.2020.01.0167. (**in Chinese**)

31. Z.Y. Zhang, S.L. Zhao, Z.P. Chen et al., Study on radiation shielding optimization method based on multi-objective evolutionary genetic algorithm. Nucl. Power Eng. **41**, 124–129 (2020). https://doi.org/10.13832/j.jnpe.2020.S1.0124. (**in Chinese**)

32. Y.H. Li, T. Yu, Z.P. Chen et al., Development and verification of radiation shielding optimization design platform for marine reactor. Nucl. Power Eng. **43**, 208–214 (2022). https://doi.org/10.13832/j.jnpe.2022.01.0208. (**in Chinese**)

33. H.J. Zhang, Z.P. Chen, C.W. Liu et al., Study on many-objective optimization method for reactor 3D shielding structure based on genetic algorithm. Nuclear Techniques (in Chinese) **45**, 110603 (2022). https://doi.org/10.11889/j.0253-3219.2022.hjs.45.110603

34. R.H. Stewart, T.S. Palmer, B. DuPont, A survey of multi-objective optimization methods and their applications for nuclear scientists and engineers. Prog. Nucl. Energy **138**, 103830 (2021). https://doi.org/10.1016/j.pnucene.2021.103830

35. Y.M. Song, Z.H. Zhang, J. Mao et al., Research on fast intelligence multi-objective optimization method of nuclear reactor radiation shielding. Ann. Nucl. Energy **149**, 107771 (2020). https://doi.org/10.1016/j.anucene.2020.107771

36. J. Wang, S.C. Liu, M.C. Li et al., Multiobjective genetic algorithm strategies for burnable poison design of pressurized water reactor. Int. J. Energy Res. **45**(8), 11930–11942 (2021). https://doi.org/10.1002/er.5926

37. S.W. Guo, Z.P. Chen, X.B. Jiang et al., Study on neutronic/thermal-mechanical coupling calculation method for fast-neutron pulse reactor with metallic nuclear fuel. Nucl. Power Eng. **43**(4),

31–37 (2022). https://doi.org/10.13832/j.jnpe.2022.04.0031. (**in Chinese**)

38. Y.G. Ma, M.Y. Liu, B.H. Xie et al., Neutronic and thermal-mechanical coupling analyses in a solid-state reactor using Monte Carlo and finite element methods. Ann. Nucl. Energy **151**, 107923 (2021). https://doi.org/10.1016/j.anucene.2020.107923

39. M.H. Weng, S.C. Liu, Z.H. Liu et al., Development and application of Monte Carlo and COMSOL coupling code for neutronics/thermohydraulics coupled analysis. Ann. Nucl. Energy **161**, 108459 (2021). https://doi.org/10.1016/j.anucene.2021.108459

40. S.W. Guo, Z.P. Chen, X.B. Jiang et al., Effect of reflected neutrons for fast pulsed reactor characteristics with metallic nuclear fuel. Nuclear Techniques (in Chinese) **47**, 060602 (2024). https://doi.org/10.11889/j.0253-3219.2024.hjs.47.060602

41. Ž. Štancar, L. Snoj, L. Barbot, Reaction rate distribution experiments at the Slovenian JSI TRIGA Mark II research reactor. *International Handbook of Evaluated Reactor Physics Benchmark Experiments* (TRIGA-FUND-RESR-002 Paris, 2017)

42. B.A. Gurovich, E.A. Kuleshova, Y.I. Shtrombakh et al., Fine structure behaviour of VVER-1000 RPV materials under irradiation. J. Nucl. Mater. **389**, 490–496 (2009). https://doi.org/10.1016/j.jnucmat.2009.02.002

43. Z.Q. Wu, J.S. Xie, L. Lou et al., Control rod strategy for long-term small rod-controlled pressurized water reactors. Nuclear Techniques (in Chinese) **47**, 030604 (2024). https://doi.org/10.11889/j.0253-3219.2024.hjs.47.030604

44. Y.J. Fu, T. Yu, J.H. Ye, Energy-endowed kinetic chromatographic columns for rapid uranium extraction from seawater. Nuclear Techniques (in Chinese) **47**, 020603 (2024). https://doi.org/10.11889/j.0253-3219.2024.hjs.47.020603

45. K. Kobayashi, N. Sugimura, Y. Nagaya, 3D radiation transport benchmark problems and results for simple geometries with void region. Prog. Nucl. Energy **39**, 119–144 (2001). https://doi.org/10.1016/S0149-1970(01)00007-5

46. A.K. Sun, Z.P. Chen, L.J. Kuang et al., Development and verification of a Monte Carlo calculation program magic for dose of Boron Neutron Capture Therapy. Modern Appl. Phys. **14**, 41–48 (2023). https://doi.org/10.12061/i.issn.2095-6223.2023.040202. (**in Chinese**)